Pressure-induced and flaring photocatalytic diversity of ZnO particles hallmarked by finely tuned pathways

Martina Vrankić,[a,*] Ankica Šarić,[a,*] Takeshi Nakagawa,[b] Yang Ding,[b] Ines Despotović,[c] Lidija Kanižaj,[d] Hirofumi Ishii,[e] Nozomu Hiraoka,[e] Goran Dražić,[f] Dirk Lützenkirchen-Hecht,[g] Robert Peter[h] and Mladen Petravić[h]

[a]*Division of Materials Physics and Center of Excellence for Advanced Materials and Sensing Devices, Ruđer Bošković Institute, Bijenička 54, 10000 Zagreb, Croatia.* mvrankic@irb.hr, Ankica.Saric@irb.hr

[b]*Center for High-Pressure Science & Technology Advanced Research, 100094 Beijing, P.R. China.* takeshi.nakagawa@hpstar.ac.cn, yang.ding@hpstar.ac.cn

[c]*Division of Physical Chemistry, Ruđer Bošković Institute, 10000 Zagreb, Croatia.* Ines.Despotovic@irb.hr

[d]*Division of Materials Chemistry, Ruđer Bošković Institute, 10000 Zagreb, Croatia.* Lidija.Kanizaj@irb.hr

[e]*National Synchrotron Radiation Research Center, Hsinchu 30076, Taiwan.* *h_ishii@spring8.or.jp*, *hiraoka@spring8.or.jp*

[f]*Department of Materials Chemistry, National Institute of Chemistry, Hajdrihova 19, Ljubljana, Slovenia.* goran.drazic@gmail.com

[g]*Fk. 4, Physik, Bergische Universität Wuppertal, Gauss-Straße 20, D-42097 Wuppertal, Germany.* dirklh@uni-wuppertal.de

[h]*University of Rijeka, Department of Physics and Centre for Micro- and Nanosciences and Technologies, Radmile Matejčić 2, 51000 Rijeka, Croatia* rpeter@phy.uniri.hr, mpetravic@phy.uniri.hr

Corresponding authors at: Division of Materials Physics and Center of Excellence for Advanced Materials and Sensing Devices, Ruđer Bošković Institute, Bijenička 54, 10000 Zagreb, Croatia.
E-mail address: mvrankic@irb.hr (Martina Vrankić), Ankica.Saric@irb.hr (Ankica Šarić)
Phone: +385 1 456 1120

Abstract

To optimize the properties of shape-selected ZnO particles for flexible and reliable applications, it is necessary to control their microstructure and morphology. In particular, finely tuned ZnO nano/microstructures of different sizes and shapes should be further chemically manipulated as desired, and the integration of chemical understanding and physical measurement with scientific theory is required. Herein, we delivered a detailed description of the mechanism that mimics the formation of finely-tuned, spherical ZnO nanoparticles (NPs) at the computational level. We tackled issues that significantly affect the favorable structural motifs of the spherical ZnO NPs grown hydrothermally from ethanolic solution leading to their advancing chemical and physical properties. The excellent photocatalytic activity of the spherical ZnO was addressed by an apparent-rate constant of $9.7(2)x10^{-2}$ min^{-1} efficiently degrading the Rhodamine B solution by ~99 % in 50 min. The apparent-rate constant for spindle-like ZnO nanoparticles is almost six times lower than that of spherical ZnO particles. Comparative results revealed that the diversity of size and shape of ZnO particles distinguishes the wurtzite-to-rocksalt transformation reversibility phenomena by dictating the microstructure-dependent deformation behavior and ultimately leading to different transition-induced elastic strain responses to hydrostatic pressure up to 29 GPa.

Keywords: high pressure; X-ray diffraction; microstructure; phase transition; oxide materials; catalysis

1. Introduction

Given the rising interest in ZnO-based applications, the definition of the most optimal preparation route is a timely subject as it is one of the most important loops to be circumvented in the strategic design for the rational and cost-effective fabrication of functionalized ZnO-based materials. Undoubtedly, intensive ZnO-based nanotechnology has witnessed a topping advancement over the last decades [1-6]. A powerful combination of unique optical, semiconducting, piezoelectric, and catalytic properties [7,8] fused with thermal and chemical stability [9], as well as both biocompatible and biodegradable peculiarities [10] leads to superior functionality [11,12] of ZnO-based nanomaterials. At the same time, the ZnO NPs, which occur, in a wide range of morphologies [13], have been rediscovered as innovative agents for medical applications. In their 2020 outlook, Wiesmann, Tremel, and Briegera outlined a breakthrough role

of ZnO NPs as pioneering anti-tumor agents in cancer medicine [14]. Based on their great prerequisites, several research groups [15,16], reported the successful binding of ZnO NPs with the COVID-19 targets, *via* the formation of hydrogen bonds, and highlighting the competence of the ZnO NPs strongly related to the effects of microstructure and morphology.

Apart from the significant superiority and better performance of ZnO NPs over other antiviral metal oxides NPs, a serious weakness of pure ZnO NPs is their rather poor application in the photodegradation processes of dye pollutants, such as Rhodamine B (RhB, $C_{28}H_{31}ClN_2O_3$) and/or Methylene Blue (MB, $C_{16}H_{18}N_3SC$), which further limits large scale-application of this family of semiconducting oxides. Indeed, the main drawback of the efficient photocatalytic activity of ZnO and the enhanced quantum yield is manifested in a very small apparent first-rate constant, k_{app}, due to the rapid recombination of photogenerated electrons and holes [17,18]. A recent review of the literature collection on this particular topic showed that Pirashemi et al. (2015) published the degradation rate constants of RhB dye over the ZnO and ZnO/Ag_2CrO_4 catalysts of 13.3×10^{-4} and 213×10^{-4} min^{-1}, respectively, indicating that the activity of the ZnO/Ag_2CrO_4 nanocomposite was about 16 times larger than that of pure ZnO [19]. Neena and co-workers (2018) published the value of the rate constant of 9.16×10^{-4} min^{-1} for the Fe-Cd co-modified ZnO over RhB dye solution, which is ~3.7 times higher than that of pure ZnO [20]. Recent findings, by Ma et al. (2021), estimated from the photocatalytic degradation kinetics of pure ZnO and Ar–H plasma-modified ZnO catalysts over RhB dye pollutant, highlighted a degradation rate of Ar–H plasma-modified ZnO, 20 times greater than that of pure ZnO, with k_{app} values of 8.933×10^{-2} min^{-1} for Ar–H plasma-modified ZnO and only 3.96×10^{-3} min^{-1} for pure ZnO [21]. Interestingly, there has been no report on the synthesis of pure ZnO photocatalyst with highly efficient photodegradation activity, despite extensive attempts in this field. Chemically, the surface of ZnO NPs is rich in -OH groups, which can be easily decorated and functionalized by various surface decorating molecules [22,23]. It is important to note that the reactivity of ZnO NPs in most applications arises from their interaction with an aqueous medium. However, a thorough understanding of the interaction of ZnO NPs with H_2O at the atomic level is still lacking. The large affinity of H_2O molecules for ZnO NPs leading to the spontaneous dissociation of H_2O was demonstrated by the Petridis group [24]. Šarić et al. reported a strong influence of the synthesis

route on the formation of ZnO NPs, their size, and geometrical shape in several recent papers [25-29].

As a highly attractive material with exceptional semiconducting, piezoelectric, and pyroelectric properties, addressing the joint chemical and physical properties (i.e. high-pressure experimental data on strain/stress, crystallite size, and shape) of ZnO NPs is extremely important for further implementation in various industries. Elucidating the effects of both, microstructure [30] and morphology [31-33] on the properties of ZnO under high pressure is a foundation for exploring the physical and chemical mechanisms that govern the intertwined structure–property relationships. The structure of ZnO at ambient conditions adopts the space group symmetry $P6_3mc$ (a=3.25224(7) Å, c=5.20955(12) Å, V=47.72 Å^3) [34] consisting of two interpenetrating hexagonal-closed-packed (hcp) sublattices (i.e. wurtzite structure, *w*) and can be driven by external hydrostatic pressure into a cubic arrangement (i.e. rock salt structure, *rs*) with F-43m space group setup (a=4.489 Å, V=90.46 Å^3) [35]. The pressure-induced hexagonal to cubic phase transition in ZnO occurs at a relatively modest pressure of ~10 GPa and is accompanied by a large volume decrease of about 17 %, as reported by Bates et al. in their seminal 1962 study [36]. Much work has been done on the high-pressure behavior of the bulk ZnO along with the structural stability and reversibility of the phase transition processes [36-43], but there are still some critical obstacles that need to be elucidated, both experimentally and theoretically. In particular, the establishment of the methodology to physically control the reversibility of the *w* to *rs* phase transition by external pressure stimuli and the direct construction of shape-selected ZnO NPs, i.e. morphology-controlled ZnO synthesis routes, by developing the theoretical mechanisms that can control the specific functionality, remain to be elucidated.

This work takes a fresh look at the physical and chemical peculiarities of shape-selected ZnO particles prepared by different routes, concisely elaborating the mechanical response to external hydrostatic pressure via Synchrotron Powder X-ray diffraction (SPXRD) experiments and the enhanced degradation kinetics over RhB dye pollutant. The characterization panorama is further implemented with results from Transmission Electron Microscope (TEM) and Scanning Electron Microscope (SEM) micrographs and X-ray Photoelectron Spectroscopy (XPS) fingerprints, which provide a detailed insight into the morphological versatility and surface diversity of synthesized ZnO polycrystals. Herein, we have mimicked theoretical breakthroughs at the Density Functional Theory (DFT) level leading to morphology-driven ZnO NPs, reflecting

enhanced catalytic activity and pressure-induced internal strain contributions to the mechanical properties of nanocrystalline ZnO particles.

2. Experimental

2.1 Materials and Synthesis

Zinc acetylacetonate monohydrate [$Zn(C_5H_7O_2)_2 \cdot H_2O$; *Alfa Aesar,* Germany], sodium hydroxide (NaOH; *Kemika,* Croatia), triethanolamine ($C_6H_{15}NO_3$; *Fisher Chemical*, USA), absolute ethanol (CH_3CH_2OH; *J. T. Baker*, Netherlands), and 1-octanol [($CH_3(CH_2)_7OH$; *Sigma Aldrich*, Germany], all in analytical purity, were used to prepare the samples. Double distilled water was prepared in our laboratory. Hydrothermal syntheses of ZnO NPs were carried out in the presence of triethanolamine (TEA) using CH_3CH_2OH (sample et_ZnO) and $CH_3(CH_2)_7OH$ (sample ot_ZnO) following the procedure described in more detail in ref. [26]. A typical synthesis of the calc_ZnO sample involved dissolving a defined amount of $Zn(acac)_2 \cdot H_2O$ (2.0 g) in aqueous NaOH solution (200 ml) according to the procedure described in [25].

2.2 Powder X-ray diffraction (PXRD) measurements at ambient conditions

PXRD measurements at RT were collected in reflection mode using a monochromatic Cu Kα X-ray source (λ = 1.54056 Å) on a Philips PW1880 diffractometer with a step size of 0.02° in the 2θ range between 10° and 70°.

2.3 In-situ SPXRD experiments at non-ambient conditions

The *in situ* SPXRD experiments were performed on the Taiwanese BL12B2 sector of SPring-8 facility (Hyogo, Japan). Two wide-opening Diamond Anvil Cells (DACs) with 4 pins and shallow DAC with 3 pins were prepared for pressurization with diamond anvils of 400 mm culet diameter. Each finely ground powder sample was compressed into a small pellet and loaded along with a ruby sphere into a stainless steel gasket of defined pre-pressed thickness and drilled hole. SPXRD measurements were collected at RT in axial geometry. Details are summarized in the Supplementary Information. Silicone oil was used as the pressure-transmitting medium and each pressure point was determined by the matching pressure shift of the ruby fluorescence line [44]. A monochromatic X-ray beam with a wavelength of 0.5657 Å was used as the probe source.

The sample-detector distance and other parameters of the detector were calibrated using the CeO_2 standard. Diffraction patterns were recorded using a Charge-Coupled Device (CCD) image plate detector (0.073 × 0.073 mm/pixel). Two-dimensional diffraction patterns were integrated into one-dimensional profiles with an IPAnalyzer and peak positions were determined semi-automatically with PDIndexer software [45].

Structure refinements against one-dimensional diffraction data were performed with the Rietveld algorithm [46] using the X'Pert HighScore Plus program [47]. A pseudo-Voigt profile function and a polynomial background with up to six coefficients were applied to the structure refinements. Crystallite size and lattice microstrain information were extracted from the phase fitting method (i.e. simultaneously with the Rietveld structure refinements) based on the change in profile widths compared to a standard sample. The tensor surfaces were additionally evaluated and interpreted using a generalized model for the broadening of microstrain peaks within the GSAS II software [48]. Quantitative phase analysis was performed using the formalism described by Hill and Howard [49]. For each phase, all compression data points were fitted with the third-order Birch-Murnaghan Equation of State (EOS) [50] using EosFit7 software [51]. A realistic estimate of the compression parameters is given by the following formula:

$$\boldsymbol{p} = \frac{\mathbf{3}}{\mathbf{2}}\boldsymbol{B_0}\left[\left(\frac{\boldsymbol{V_0}}{\boldsymbol{V}}\right)^{\frac{\mathbf{7}}{\mathbf{3}}} - \left(\frac{\boldsymbol{V_0}}{\boldsymbol{V}}\right)^{\frac{\mathbf{5}}{\mathbf{3}}}\right]\left\{\mathbf{1} - \frac{\mathbf{3}}{\mathbf{4}}(\mathbf{4} - \boldsymbol{B_0'}) \times \left[\left(\frac{\boldsymbol{V}}{\boldsymbol{V_0}}\right)^{\frac{\mathbf{3}}{\mathbf{4}}} - \mathbf{1}\right]\right\} \quad (1)$$

where B_0 is isothermal bulk modulus at atmospheric pressure, $\boldsymbol{B_0'}$ is its pressure derivative ($\equiv dB_0/dP$), and V_0 is the unit cell volume at zero pressure.

2.4 Surface morphology imaging

Morphological analysis was performed using a Field Emission Scanning Electron Microscope (FE-SEM) JSM-7000F and a Cs-corrected probe Cold Field Emission (CFE) Scanning Transmission Electron Microscope (STEM) Jeol ARM 200 CF. A low beam current and electron energy of 80 keV were used to minimize the beam damage. High-Angle Annular Dark-Field (HAADF) images were acquired using 68-180 mrad collection half-angles at 24 mrad probe convergence semi-angles. The Gatan Quantum ER dual Electron Energy-Loss Spectroscopy (EELS) and Jeol Centurio Energy Dispersive X-ray Spectroscopy (EDXS) system with 100 mm^2 Silicon Drifted Detector (SDD) were used for chemical analysis. The powder samples were directly transferred to the lacey carbon-coated nickel STEM grids.

2.5 Photocatalytic activity measurements

Photocatalytic activity of the samples was monitored by photodegradation of aqueous RhB dye under ultraviolet (UV) light. For each reaction, 3 mg of the powder sample was dispersed in a 3.0 ml of 10 ppm aqueous RhB dye solution. Before irradiation with UV light, the suspension was sonicated for 5 min and stirred constantly for 1 h in the dark to achieve adsorption−desorption equilibrium between the dye solution and the photocatalyst. Then, eight UV lamps of 352 nm (8 watt, Hitachi) were turned on to start photodegradation in a photoreactor (Luzchem LZC-4V). A magnetic stirrer was placed at the bottom of the cell containing the reaction mixture to maintain homogeneity. After the suspension was kept under UV light irradiation, a certain amount of the sample (2 mL) was taken at fixed time intervals (20 min) and centrifuged at 7000 rpm for 8 min. Photocatalytic degradation reactions were monitored by measuring the concentration of a degraded supernatant liquid as a function of irradiation time by UV-Visible (UV-Vis) absorption spectra using a UV-Vis spectrophotometer (Varian Cary 50). Blank experiments were performed without the photocatalysts. The extracted information from the RhB dye solution photocatalytic degradation curves allowed the determination of the reaction type and the calculation of the kinetic constant of the RhB pollutant solution degradation reaction. All experiments were conducted at RT. The degradation rate *r* of the RhB dye solution can be expressed as [52]:

$$r = -d(C)/dt = k_{app}(C)^n \quad (2)$$

where *C* is the concentration of RhB pollutant molecules, k_{app} is the apparent-rate constant and *n* is the order of the reaction. The absorbance at 554 nm was used to calculate the amount of RhB dye solution that degraded with time. The percentage of degradation was calculated using the following formula [53]:

$$Degradation\ \% = [(C_0 - C_t)/C_0] \times 100 \quad (3)$$

where C_0 and C_t are the initial concentration and the concentration after exposure to UV light at time *t*, respectively. The k_{app} was calculated using the slope of the graph of ln C_0/C_t versus the irradiation time.

2.6 X-ray photoelectron spectroscopy measurements

The chemical composition of the surface was investigated using a SPECS laboratory XPS system under UHV conditions (the typical pressure was in the range of 10^{-7} Pa) with Al Kα X-rays of 1486.74 eV and the Phoibos100 electron energy analyzer. The pass energy

was set to 10 eV, resulting in a total energy resolution of about 0.8 eV. The experimental spectra were fitted with the Gaussian-Lorentzian functions after the Shirley background subtraction [54].

2.7 Computational methods

Geometry optimizations were performed with quantum chemical calculations at the DFT level using the Gaussian 09 program (revision D1) [55]. The $(ZnO)_{36}$ cluster served as a credible model for all possible molecular surface/solvent and surface/TEA additive interaction predictions [56]. Solvent effects (CH_3CH_2OH, ε=24.85; $CH_3(CH_2)_7OH$, ε=9.86; H_2O, ε=78.36) were accounted for using the implicit Solvation Model Based on Density (SMD) polarizable continuum [57]. The M05-2X functional [58] developed by the Truhlar's group was used. The mixed 6–31+G(d,p) + LANL2DZ basis set was used for geometry optimization, while the Pople's 6–31+G(d,p) double-ξ basis set and LANL2DZ basis [59] were chosen for the H, C, O, N and Zn atoms, respectively. The final single-point energies were refined using a highly flexible 6–311++G(2df,2pd) basis set for the H, C, O, and N atoms, while the same ECP-type LANL2DZ basis set was used for the Zn atoms. Bader's Quantum Theory of Atoms in Molecules (QTAIM) [60] coupled with the AIMALL software package [61] was employed for the topological analysis of electron density. The chemical bond type was qualitatively described by the sign and values of the electron density Laplacian $\nabla^2\rho(r_c)$ and the electron energy density $H(r_c)$ at the corresponding bond critical point. The interaction free energies, ΔG^*_{INT}, were calculated as the difference between the total free energy (G^*_{AB}) of the resulting structures and the sum of the total free energies ($G^*_A + G^*_B$) of the associating units.

3. Results and discussion

3.1 Structural and microstructural response to pressure at room temperature

The resulting white polycrystals of et_ZnO, ot_ZnO, and calc_ZnO exhibited single-phase SPXRD patterns at RT and slightly elevated pressures of 0.10 GPa, 0.36 GPa, and 0.50 GPa, respectively, preserving exclusively the crystal structure of hexagonal pristine *w*-ZnO with $P6_3mc$ space group symmetry [34] as indicated from the Rietveld refinements

(Fig. 1) and as shown in the Supplementary Information (see Fig. S1 and Fig. S2). The resulting unit cell metrics are summarized in Table S1, along with reliability factors that confirm the validity of the refinement. However, when the pressure reached 13.16 GPa, 15.73 GPa, and 12.44 GPa in et_ZnO, ot_ZnO, and calc_ZnO, respectively (Fig. 1b, Fig. 1d and Fig. S2), the *in situ* axial X-ray diffraction (AXRD) profiles revealed the appearance of a new set of reflections not indexed by the hexagonal structural model. The presence of cubic (111), (020), and (022) Bragg peaks clearly confirmed the *F*-43m space group assignment [35] implying the phase transition from hexagonal to cubic accompanied by a large volume collapse. As estimated from the Rietveld refinements (Table S1), the mass fraction of the cubic phase increased from 4.0 % at 13.16 GPa to 100 % at 17.68 GPa in the et_ZnO sample, a situation that persisted with further pressurization up to 29.40 GPa, the highest pressure applied in the experiments (Fig. 2a). In a remarkably similar fashion, a complete hexagonal to cubic transformation in ot_ZnO was achieved by squeezing the sample to 19.50 GPa (inset in Fig. 2a). At 15.73 GPa the mass fraction of the cubic phase in the sample ot_ZnO was 36.60 %, apparently continued to increase to 76.40 % at 16.83 GPa and finally up to 100 % at 19.50 GPa. Similarly, the mass fraction of the hexagonal phase fades at 12.44 GPa and kicks into 75.20 % of the cubic fraction in the sample calc_ZnO. A *w* to *rs* structural transition in et_ZnO completed at ~17.68 GPa resulted in a sharp ~21 % dip in unit cell volume, while compression of ot_ZnO at 19.50 GPa led to the formation of solely cubic phase and ~20 % drop in volume, resulting in consequently significant hysteresis. Diversely, a hexagonal to cubic phase transformation was revealed in calc_ZnO at 13.77 GPa, mirroring ~20 % unit cell volume collapse.

The compressibility plots of the hexagonal and cubic phases of the et_ZnO, ot_ZnO, and calc_ZnO samples are shown in Fig. 3, where the transparent solid lines are the third-order fits Birch-Murnaghan EOS [49] to the data for the *w* and *rs* phases. The fits yielded values of the bulk modules and their pressure derivatives, which are listed in Table 1. The B_0 of the *w* and *rs* phases at zero pressure were estimated to be 141(14) and 130(4) GPa for the samples prepared in alcoholic solutions. These are relatively smaller bulk moduli values compared to the values reported in some previous experiments [41,62] using Si oil as the pressure medium. Accordingly, the B_0 of the *rs* phase for et_ZnO of 215(3) and 151(2) for ot_ZnO correlate favourably with Decramps (2003) [62] and Hanna (2011) [63]. However,

since our results for calc_ZnO are based on a limited number of pressure points, the results of such analyses should consequently be treated with the utmost caution.

The high pressure phases of both, et_ZnO and ot_ZnO were stable up to ~29 GPa. Interestingly, the fingerprints of the cubic diffraction patterns did not reappear during decompression from ~29 GPa to 0 GPa – hexagonal structures were retained beyond the upward transition pressure in both et_ZnO and ot_ZnO samples. Such experimental results for the structural transitions in prepared ZnO samples correlate well with data published for bulk ZnO [36,39,64,65] and further support the concept of first-order solid-state transformation in prepared ZnO samples. In contrast, a very different trend was observed for the calc_ZnO sample after depressurization (Fig. 1d). Namely, the calc_ZnO sample undergoes a first-order pressure-induced phase transformation at 12.44 GPa, followed by the transition zone imaged up to 13.77 GPa and accompanied by a ~20 % volume decrease (Fig. 3). In contrast to et_ZnO and ot_ZnO, a reversible pressure-induced phase transition to single-phase hexagonal symmetry was observed in the calc_ZnO sample by slowly depressurizing from 15.46 GPa to ambient pressure (Fig. 1d and Fig. 4). Nevertheless, the phase transitions in all prepared samples followed a two-step hexagonal path [66], which was accompanied by a pronounced linear decrease in the c/a axis ratio and further led to the formation of the cubic phase. However, it must be emphasized, that being slightly softer along the *c*-axis direction [67] even at ambient pressure (i.e. the c/a axis ratio of 1.6026(6) at 0 GPa, is smaller than the ideal value [68] of 1.633) the hexagonal packing shows a minor indication of an abnormal variation of the c/a axis ratio near the structural transition pressure. This further leads to a slight deviation of the position parameter u from the ideal $uc/a=(3/8)^{1/2}$ as the hexagonal packing becomes denser. The observed changes in the $d(100)/d(002)$ ratio for the hexagonal phase and the $d(020)/d(220)$ ratio for the cubic phase correlate highly with the pressure variations over the studied range in et_ZnO, ot_ZnO, and calc_ZnO (see Fig. 4). Specifically, the ratio $d(100)/d(002)$ increases linearly with pressure before the phase transformation and deviates from the linear relationship in the transition zone, while the ratio $d(020)/d(220)$ decreases slightly with pressure after the phase transition. Such anisotropic compression behavior indicates that both *w*-ZnO and *rs*-ZnO phases are distorted in the transition zone, as discussed previously in ref. [30].

Since the transformation reversibility of the *rs*-ZnO phase is a rather contradictory phenomenon [36-40,69,70] it has been a central issue for a long time, with a quite puzzling question to be addressed - why do the phase-pure ZnO samples of the cubic assemblies show

different transformation activities under the same pressure ranges? While some previous experiments showed that the transition from *rs* phase to *w* phase returns to *rs* phase with pronounced hysteresis [36,37,39] other experiments showed that the partially extinguished *rs* phase persists with *w* phase at ambient conditions. Essentially, such delicate behavior results from the involved surface energy differences [30,64] between the crystalline phases and the volume collapse ratio. Particle size effects significantly affect the pressure range of phase stability and the final fractions of *rs* and *w* phases at ambient conditions [30] in various ZnO samples. As suggested by Liu et al. [42] a plausible explanation for such different reversibility phenomena observed in et_ZnO, ot_ZnO, and calc_ZnO is a small amount of the *rs* phase trapped in the nanoscale grain size during the *w* to *rs* transition upon compression and then the *rs* to *w* transition upon decompression, resulting in the partial visibility of the *rs* phase even after the pressure is released. Moreover, the mechanism of pressure hysteresis strongly reflects the effects of crystallite size and lattice strain [71-75]. Remarkably, Fig. 5a shows a clear trend – the higher the pressure, the more pronounced the reduction in crystallite size. The most striking observation that emerges from the comparison of the et_ZnO, ot_ZnO, and calc_ZnO data is an abrupt change in crystallite size in the calc_ZnO sample, observed from 94.1(1) at 0 GPa to 62.2(1) at 0.36 GPa. In contrast, no significant difference in crystallite size values was observed in the other two ZnO samples over such a very narrow pressure range.

Together with the mapping of the surface morphology at ambient conditions (see Fig. S3), the results of the line broadening analysis (Fig. 5) supported a significant insight into the role of the compression behavior of the high-pressure phases in ZnO samples, i.e. the crystallites formed in the calc_ZnO sample are larger, implying a smaller surface area [76] and thus favoring a reversible transformation process from cubic to hexagonal symmetry upon decompression. On the other hand, the much smaller crystallites of 45.9(1) and 18.9(1) size in et_ZnO and ot_ZnO, respectively, promote a rather striking stability of the cubic lattice and potentially hinder the transformation process upon decompression to 0 GPa. In general, the higher phase transition pressure compared to the bulk is consistent with previous results [30] and is attributed to the large surface-to-volume ratio [77] of the nanocrystals. Independent of the contribution of the crystallite size, the phase transition process is also largely related to the transition-induced elastic strain [65] arising from the lattice differences between hexagonal and cubic phases. Based on the Rietveld refinements, the evolution of lattice microstrain as a function of applied pressure in et_ZnO,

ot_ZnO, and calc_ZnO did not show the same trend of change over the same pressure range, as shown in Fig. 5. Prior to the hexagonal to cubic phase transition, the average lattice microstrain increases with pressure in an almost exponential manner in both hydrothermally produced and calcined ZnO samples. At the onset of the phase transition, the lattice strain in the sample et_ZnO decreases steeply with pressure indicating the occurrence of plastic flow [78], which leads to a further decrease in the strength of each phase, thus showing similarities with commercially available polycrystalline ZnO powder, such as ref. [30]. The occurrence of plastic flow can relax the internal strain, allowing further growth of the cubic phase [78,79]. On the other hand, at low pressure, there is a pure hexagonal phase with large lattice strain in both the ot_ZnO and calc_ZnO samples, while a jump in strain is visible during the phase transition. After the phase transition, the lattice microstrain remains relatively stable at higher pressures in all prepared samples. Undoubtedly, a larger microstrain reduces the crystallite size, strengthens the bond bending, and thus has a strong influence on the reversibility phenomena and mechanical properties of the ZnO particles [80,81].

3.2 Photocatalytic degradation of RhB dye

As shown in the left panel of Fig. 6, the sample et_ZnO exhibits the highest photocatalytic activity towards the RhB pollutant, a carcinogenic textile dye. Namely, a significant increase in photocatalytic activity towards photodegradation of RhB footprints was observed for photocatalysts ot_ZnO and et_ZnO under UV irradiation with a duration of 50 min compared to sample calc_ZnO, where complete degradation occurred only after a treatment time of 200 min. The blank test was the RhB dye solution (Fig. S4), directly illuminated by a UV source without catalyst. In general, the RhB solution is quite stable once illuminated [21] – negligible wavelength shifts and absorption peak intensities are observed under illumination, while the addition of et_ZnO, ot_ZnO and calc_ZnO photocatalysts leads to a steep decrease in adsorption at 554 nm with irradiation time. Based on a comparison of the regression coefficients, R^2, the photocatalytic dye degradation reaction is assumed to follow first-order kinetics (Table 2), which ensures the model Langmuir–Hinshelwood [82]. The photocatalytic RhB degradation rates using different ZnO catalysts are tabulated in Table 2. As shown in Fig. 6e, the apparent rate constants of

the products increased from 1.56(1) $\times 10^{-2}$ min^{-1} to 9.7(2) $\times 10^{-2}$ min^{-1}, in the order calc_ZnO>ot_ZnO>et_ZnO, while k_{app} was only 5×10^{-4} min^{-1} in the blank experiment.

Various efforts have been made to improve the photocatalytic activity of ZnO catalysts by modifying their surface and structure [21,83-93], but to our knowledge no other author has found such a high first-order rate constant for a pure ZnO photocatalyst prepared by the methods we described in this study. Our results differ significantly from previous results reported in the literature, where the degradation rate of the RhB solution was improved after the addition of pure ZnO, but still showed rather poor degradation activity, with k_{app} in the range of 3.96×10^{-3} to 2.5×10^{-2} min^{-1} [21,88]. The et_ZnO sample showed the best photocatalytic activity (Fig. 6f) for RhB dye degradation in 50 min (about 99 % degradation). At the same time, degradation with ot_ZnO and calc_ZnO was found to be high 98 % and significantly low 53 %, respectively. It is critical to note that the result for the et_ZnO degradation effect over the RhB dye solution is comparable to the result reported for the plasma modified [21] ZnO NPs, which efficiently degraded the RhB solution by 97.8 % in 40 min.

3.3 Surface diversity of ZnO samples identified by XPS characterization

Photoemission spectra around the O 1s core-levels of et_ZnO, ot_ZnO and calc_ZnO are shown in Fig. 7. All spectra show a similar structure: the main peak at the binding energy (BE) of 530.0 eV and a smaller feature shifted to a higher BE of 531.5 eV. We assign the dominant line to the O 1*s* emission corresponding to electrons from the Zn-O bonds (O^{2-} ions) originating from oxygen of the ZnO crystal lattice [85,94]. On the other hand, the additional peak at 531.5 eV is attributed to oxygen or hydroxide species [95]. Indeed, the physically absorbed OH radicals ($^{\bullet}OH$) [96] are an important active species in semiconductor photocatalysis. The relative fraction of the chemisorbed O or OH groups is largest in the et_ZnO sample, with a relative contribution of 30 % (compared to 23 % in calc_ZnO and 21 % in ot_ZnO). We explain this difference by a higher adsorption affinity for O or OH species on the et_ZnO surface, which in turn may contribute to the enhanced photocatalytic activity observed for this sample. Indeed, the amount of O or OH species on surfaces of photocatalytic materials was previously found to play an important role in the photocatalytic activity, leading to more efficient photocatalytic activity on surfaces with a higher

concentration of oxygen or •OH. The difference in the atomic structures of the surfaces may lead to the discrepancy in the ability of chemisorbed oxygen species or •OH [97,98].

3.4 Understanding the mechanism of ZnO NPs formation towards diverse high pressure behavior and enhanced photocatalytic activity

Undoubtedly, the use of various synthesis methods can modify both the microstructure and morphology of ZnO NPs and their chemical and physical properties, thus playing an important role in controlling the catalytic performance and mechanical properties towards improved functionalities and direct applications of this material. The mechanism governing the formation of ZnO particles has been deciphered by detailed theoretical simulations of ZnO interface-solvent and interface-additive interactions using quantum chemical calculations. In particular, we identified the mechanism of ZnO particle formation in the desired ZnO catalyst by integrating various synthetic chemistry and materials physics data (i.e. microstructure and surface behavior) using theoretical simulations of the ZnO surface/solvent and surface/additive interactions using $(ZnO)_{36}$─H_2O, $(ZnO)_{36}$─CH_3CH_2OH, $(ZnO)_{36}$─$CH_3(CH_2)_7OH$, and $(ZnO)_{36}$─TEA models (Fig. S5). The $(ZnO)_{36}$ cluster served as a suitable model [61] for cluster modeling. The most stable $(ZnO)_{36}$─H_2O-, $(ZnO)_{36}$─CH_3CH_2OH-, $(ZnO)_{36}$─$CH_3(CH_2)_7OH$- and $(ZnO)_{36}$─TEA-structures, as well as the bond lengths(d), energies (E), and QTAIM properties of the selected bonds are summarized in Table S2. The calculated values of the Gibbs free energies of the surface/additive interaction are given in Table S3, while the total electronic energies, thermal corrections to the Gibbs free energy, total free energies of the resulting and associating unit structures are given in Table S4. The primary ZnO NPs in the ot_ZnO sample showed a high tendency to spherical aggregation, while no significant tendency to spherical aggregation of fine uniform NPs was observed in the ethanol media. Most likely, such treatment enables a sufficient combination of favorable electrostatic interaction between ZnO NPs, small polar molecules of ethanol, and the smaller amount of TEA molecules, to prevent the aggregation process. However, the aggregation of fine primary ZnO NPs into larger densely packed spheres in ethanol media is favored by increasing the TEA concentration, indicating the shaping role of TEA chains in stimulating the aggregation process [26,99]. Because of the ability of ethanolamines to combine the

properties of amines and alcohols and to participate in reactions common to both groups, resulting in a considerable change in particle surface properties, good control of morphology and crystallite size is achieved by changing the nature of the alcoholic solvents and the molar ratio [TEA]/[$Zn(acac)_2$]. Consequently, it appears that a small amount of TEA suppresses both the growth of the primary NPs and their assembly (sample et_ZnO), while the excess amount of TEA suppresses the growth of the primary NPs and mimics a bridge between adjacent ZnO NPs to form the large, spherical ZnO agglomerates (sample ot_ZnO). The influence of the TEA additive on the overall shape of the ZnO NPs and their aggregates in both et_ZnO and ot_ZnO samples was confirmed by theoretical simulations of the surface/additive interactions using an appropriate $(ZnO)_{36}$─TEA model.

The calculated values of Gibbs free energies showed that the $(ZnO)_{36}$─TEA interaction is a spontaneous exergonic process in both CH_3CH_2OH and $CH_3(CH_2)_7OH$ solvents, with Gibbs energy values of ΔG^*_{INT}=-8.52 kcal mol^{-1} and ΔG^*_{INT}=-7.68 kcal mol^{-1}, respectively (see Table S2). However, the possible surface/solvent $(ZnO)_{36}$─CH_3CH_2OH or $(ZnO)_{36}$─$CH_3(CH_2)_7OH$ interactions imply the structures for which the interactions are slightly endergonic processes ($\Delta G^* > 0$). Due to the high chelating efficiency of TEA over Zn, a structural motif was observed in the $(ZnO)_{36}$─TEA model, where TEA appears to be anchored to the $(ZnO)_{36}$ cluster by three extremely strong hydrogen O─H···O bonds, which are accomplished between the hydrogen atom of TEA hydroxyl groups and the oxygen in the $(ZnO)_{36}$ cluster, increasing its stability (Fig. 8).

It is important to emphasize that the growth control of the primary ZnO NPs is ensured by the prevention of the growth of the cores and the bare ZnO NPs in the first phase due to the good adsorption of three flexible hydroxyl chains of the TEA molecules on their surfaces. Indeed, the calculated values of the binding energies indicate the unusual strength of the O─H···O-hydrogen bonds between the hydrogen atom of the TEA -hydroxyl groups with the oxygen in the $(ZnO)_{36}$ cluster, which turned out to be the most important parameter, since the control of the surface/additive interactions allows the nuclei and the bare ZnO ultrasmall NPs to grow not only along the preferred axis. As described in the literature review [83,100,101], joint experimental and theoretical studies showed a strong dependence of the photocatalytic performance on the crystal facet exposures in the order $\{0001\} > \{10\bar{1}1\} > \{10\bar{1}0\}$, with the polar {0001} being the predominant facet of the

spherical ZnO NPs. The presence of a significant amount of TEA increases the number of TEA anchor sites resulting in a higher coverage of the ZnO surface, which in turn results in higher photocatalytic efficiency of the NPs.

The calculated values of hydrogen bonding energies obtained from the surface additive interactions in the $(ZnO)_{36}$─TEA model showed that the use of ethanol as a solvent is likely to lead to much stronger bonding in the sample et_ZnO (i.e. $E_{O\cdots H}$ ranges from -39.76 kcal mol^{-1} to -40.61 kcal mol^{-}), and weaker in sample ot_ZnO (i.e. $E_{O\cdots H}$ ranges from -28.79 kcal mol^{-1} to -31.67 kcal mol^{-1}). Moreover, the aggregation process of the spherical ZnO agglomerates is mainly driven by the use of various interactions of alcoholic solvents and TEA molecules and their intermediate species with the surface of the primary ZnO NPs. Due to the high affinity of TEA and alcohol molecules for the $(ZnO)_{36}$ surface, based on the simultaneous involvement of both, a high degree of coverage is achieved and the particle size is limited on one side. On the other hand, all the free hydroxyl groups have a large capacity to attract each other through hydrogen bonding and serve as a link between the neighboring ZnO NPs. In addition, it is important to emphasize the influence of the weaker N─H···O-hydrogen bonds between the nitrogen atom of the amine group TEA and the oxygen in the $(ZnO)_{36}$ cluster on the process of spherical aggregation. In contrast, in the aqueous NaOH solution (i.e. preparation of the calc_ZnO sample), hierarchical crystal growth is present along the *c*-axis by aggregation of hollow tubular ZnO substructures with lamellar hexagonal stacking. The growth process of the hollow spindle-shaped particles is complex and has been proposed based on a combined experimental and theoretical approach. The main driving forces responsible for the preferential orientation growth along the *c*-axis of the hollow spindle-shaped particles, which is favored in the aqueous NaOH solution, are various interactions of the water-solvent molecules, as well as hydroxyl groups from NaOH, with the surface of ZnO. Interestingly, the transfer of a hydrogen atom from the water molecule to oxygen in the $(ZnO)_{36}$ cluster is observed in the most stable $(ZnO)_{36}$─H_2O structure (Table S1). As a result of this process, a free pair of electrons on the oxygen atom of the water molecule participated in a new strong coordinate bond with zinc (Zn─O): d_{Zn-O} = 2.029 Å, E_{Zn-O} = -29.15 kcal mol^{-1}. According to the topological parameters $H(r_c) < 0$ and $\nabla^2\rho(r_c) > 0$ summarized in Table S2, the Zn─O bond was assigned to an intermediate interaction type, which is a feature of coordinate bonding. Due to the

high affinity of the H_2O molecules for the $(ZnO)_{36}$ surface, which is based on the simultaneous bonding by the transfer of hydrogen atoms and the Zn─O bond, a high free energy is released (ΔG^*_{INT} = -6.74 kcal mol^{-1}). It seems that the spontaneous deprotonation of H_2O molecules, observed in the most stable $(ZnO)_{36}$─H_2O structure (Table S2), as well as the presence of NaOH where the surface of ZnO NPs is directly attacked with OH ions, play a key role in explaining the hierarchical crystal growth along the *c*-axis through the aggregation of hollow tubular ZnO substructures [102] with lamellar hexagonal stacking. The Cartesian coordinates of the calculated clusters are given in the Supplementary Information (see Tables S5 to S9).

4. Conclusions

This paper underlines the importance of bringing together theoretical understanding beyond systematic pathway set-ups leading to the design of morphologically targeted ZnO NPs. The suitability to evaluate the shape-selected ZnO NPs which are easy to compress, and concomitantly, have an excellent photocatalytic activity was tackled *via* high-pressure experiments on the order of 30 GPa and degradation measurements over the RhB dye pollutant molecules. This comparative study revealed that the diversity of size and shape of ZnO particles distinguishes the *w*-to-*rs* transformation reversibility phenomena by dictating the microstructure-dependent deformation behavior and ultimately leading to different microstrain responses to hydrostatic pressure. We have highlighted the exceptionally high apparent-rate constant of $9.7(2)\times10^{-2}$ min^{-1}, which relegates the role of spherical ZnO NPs grown hydrothermally from ethanolic solution towards the giant, spindle-shaped ZnO particles prepared in NaOH medium with calcination treatment.

It seems that by understanding the crystal growth of ZnO NPs *via* the molecular ZnO interface/solvent/additive interactions and screening the solution chemistry of ZnO NPs, one can make ZnO a highly efficient promising multifunctional material. The prospect of being able to synthesize pure ZnO NPs that efficiently degrade ~99 % of the RhB dye pollutant in 50 min serves as a continuous incentive for future research. Our results are encouraging and should be validated by a larger series of samples.

Supplementary information

Supplementary information accompanies this paper.

Authors' contributions

M.V. conceived the project, designed experiments, and contributed to conceptualization; M.V., Y.D., and D.L.H. are responsible for raising funds; A.Š. developed and optimized the synthesis method, and contributed to DFT integration in predicting the mechanism of ZnO formation; M.V. performed SPXRD characterization work; T.N. performed the high-pressure SPXRD measurements and contributed to the SPXRD analysis; H.I. and N.H. contributed to the high-pressure SPXRD experiments; I.D. performed the computational work; L.K. performed and interpreted the photocatalytic activity measurements; G.D. performed the TEM measurements; R.P. and M.P. performed and analyzed the XPS measurements. All authors contributed to the paper, which was written by M.V.

Declaration of Competing Interest

The authors declare that they have no known competing financial interests or personal relationships that could have appeared to influence the work reported in this paper.

Acknowledgments

We thank SPring-8 for providing the synchrotron radiation facilities and we thank H.I. and N.H. for assistance in the use of the beamline. M.V. gratefully acknowledges financial support from the Croatian Academy of Sciences. M.V. gratefully acknowledges the support of the project co-funded by the Croatian Government and the European Union through the European Regional Development Fund – Competitiveness and Cohesion Operational Programme (Grant KK.01.1.1.01.0001). M.V. and Y.D. gratefully acknowledge support from the bilateral project Croatian–Chinese in 2019–2021. M.V. and D.L.H. gratefully acknowledge support from the bilateral project Croatian–German(DAAD) in 2019–2021. G.D. gratefully acknowledges financial support from the Slovenian Research Agency (P2–0393). The experiments on the Taiwanese BL12B2 sector of SPring-8 were carried out under Proposal No.2018B4141 and No.2019A4132. R.P. and M. P. gratefully acknowledge support from the University of Rijeka under Project No.

18-144. The authors thank Zagreb University Computing Centre (SRCE) for generously granting computing resources on the cluster ISABELLA.

Supplementary materials

Supplementary material associated with this article can be found, in the online version.

References

1 L. Wang, M. Muhammed, Synthesis of zinc oxide nanoparticles with controlled morphology, J. Mater. Chem. 9 (1999) 2871–2878.

2 P. Sivakumar, M. Lee, Y.-S. Kim, M.S. Shim, Photo-triggered antibacterial and anticancer activities of zinc oxide nanoparticles, J. Mater. Chem. B 6 (2018) 4852–4871.

3 P. Banerjee, P.K. Jain, Mechanism of sulfidation of small zinc oxide nanoparticles RSC Adv. 8 (2018) 34476–34482.

4 D.G. Georgiadou, J. Semple, A.A. Sagade, H. Forstén, P. Rantakari, Y.-H. Lin, F. Alkhalil, A. Seitkhan, K. Loganathan, H. Faber, T.D. Anthopoulos, 100 GHz zinc oxide Schottky diodes processed from solution on a wafer scale, Nat. Electron. 3 (2020) 718–725.

5 A. Narayana, S.A. Bhat, A. Fathima, S.V. Lokesh, S.G. Suryad, C.V. Yelamaggad, Green and low-cost synthesis of zinc oxide nanoparticles and their application in transistor-based carbon monoxide sensing, RSC Adv. 10 (2020) 13532–13542.

6 P. Amuthavalli, J.-S. Hwang, H.-U. Dahms, L. Wang, J. Anitha, M. Vasanthakumaran, A.D. Gandhi, K. Murugan, J. Subramaniam, M. Paulpandi, B. Chandramohan, S. Singh, 2021. Zinc oxide nanoparticles using plant Lawsonia inermis and their mosquitocidal, antimicrobial, anticancer applications showing moderate side effects. Sci. Rep. 11, 8837.

7 Z.L. Wang, Splendid one-dimensional nanostructures of zinc oxide: a new nanomaterial family for nanotechnology, ACS Nano 2 (2008) 1987–1992.

8 P. Yang, R. Yan, M. Fardy, Semiconductor nanowire: what's next?, Nano Lett. 10 *(*2010) 1529–1536.

9 U. Ozgur, Y.I. Alivov, C. Liu, A. Teke, M.A. Reshchikov, S. Doğan, V. Avrutin, S.-J. Cho, H. Morkoçd, 2005. A comprehensive review of ZnO materials and devices J. Appl. Phys. 98, 041301.

10 J. Zhou, N.S. Xu, Z.L. Wang, Dissolving behavior and stability of ZnO wires in biofluids: a study on biodegradability and biocompatibility of ZnO nanostructures, Adv Mater. 18 (2006) 2432–2435.

11 A. Kołodziejczak-Radzimska, T. Jesionowski, Zinc Oxide—From Synthesis to Application: A Review, Materials, 7 (2014) 2833–2881.

12 B. Zhang, F. Wang, C. Zhu, Q. Li, J. Song, M. Zheng, L. Ma, W. Shen, A Facile Self-assembly Synthesis of Hexagonal ZnO Nanosheet Films and Their Photoelectrochemical Properties, Nano-Micro Lett. 8 (2016) 137–142.

13 Z.L. Wang, Nanostructures of zinc oxide, Mater. Today 7 (2020) 26–33.

14 N. Wiesmann, W. Tremel, J. Briegera, Zinc oxide nanoparticles for therapeutic purposes in cancer medicine, J. Mater. Chem. B 8 (2020) 4973–4989.

15 M. Hamdi, H.M. Abdel-Bar, E. Elmowafy, A. El-khouly, M. Mansour, G.A.S. Awad, Investigating the Internalization and COVID-19 Antiviral Computational Analysis of Optimized Nanoscale Zinc Oxide, ACS Omega 6 (2021) 6848–6860.

16 G.H. Attia, Y.S. Moemen, M. Youns, A.M. Ibrahim, R. Abdou, M.A. El Raeyh, 2021. Antiviral zinc oxide nanoparticles mediated by hesperidin and in silico comparison study between antiviral phenolics as anti-SARS-CoV-2, Colloids Surf. B Biointerfaces. 203, 111724.

17 R. Saravanan, S. Karthikeyan, V.K. Gupta, G. Sekaran, V. Narayanan, A. Stephen, Enhanced photocatalytic activity of ZnO/CuO nanocomposite for the degradation of textile dye on visible light illumination, Mater. Sci. Eng. C 33 (2013) 91–98.

18 S. Kant, D. Pathania, P. Singh, P. Dhiman, A. Kumar, Removal of malachite green and methylene blue by $Fe_{0.01}Ni_{0.01}Zn_{0.98}O$/polyacrylamide nanocomposite using coupled adsorption and photocatalysis, Appl. Catal. B 147 (2014) 340–352.

19 M. Pirhashemi, A. Habibi-Yangjeh, Novel ZnO/Ag2CrO4 nanocomposites with n–n heterojunctions as excellent photocatalysts for degradation of different pollutants under visible light, J. Mater. Sci.: Mater. Electron. 27 (2016) 4098 □4108

20 D. Neena, K.K. Kondamareddy, H. Bin, D. Lu, P. Kumar, R.K. Dwivedi, V.O. Pelenovich, X.-Z. Zhao, W. Gao, D. Fu, 2018. Enhanced visible light photodegradation activity of RhB/MB from aqueous solution using nanosized novel Fe-Cd co-modified ZnO, Sci. Rep. 8, 10691.

21 M. Pirhashemi, A. Habibi-Yangjeh, Novel ZnO/Ag_2CrO_4 nanocomposites with n–n heterojunctions as excellent photocatalysts for degradation of different pollutants under visible light, J. Mater. Sci.: Mater. Electron. 27 (2016) 4098–4108.

22 S. Ma, Y. Huang, R. Hong, X. Lu, J. Li, Y. Zheng, 2021. Enhancing Photocatalytic Activity of ZnO Nanoparticles in a Circulating Fluidized Bed with Plasma Jet, Catalysts. 11, 77.

23 D. Liu, W. Wu, Y. Qiu, S. Yang, S. Xiao, Q.-Q. Wang, L. Ding, J. Wang, Surface Functionalization of ZnO Nanotetrapods with Photoactive and Electroactive Organic Monolayers, Langmuir 24 (2008) 5052–5059.

24 F. Gao, S. Aminane, S. Bai, A.V. Teplyakov, Chemical Protection of Material Morphology: Robust and Gentle Gas-Phase Surface Functionalization of ZnO with Propiolic Acid Chem. Mater. 29 (2017) 4063–4071.

25 T.B. Rawal, A. Ozcan, S.-H. Liu, S.V. Pingali, O. Akbilgic, L. Tetard, H. O'Neill, S. Santra, L. Petridis, Interaction of Zinc Oxide Nanoparticles with Water: Implications for Catalytic Activity, ACS Appl. Nano Mater. 2 (2019) 4257–4266.

26 S. Musić, A. Šarić, Formation of hollow ZnO particles by simple hydrolysis of zinc acetylacetonate, Ceram. Int. 38 (2012) 6047–6052.

27 A. Šarić, G. Štefanić, G. Dražić, M. Gotić, Solvothermal synthesis of zinc oxide microspheres, J. Alloys Compd. 652 (2015) 91–99.

28 A. Šarić, I. Despotović, G. Štefanić, G. Dražić, The Influence of Ethanolamines on the Solvothermal Synthesis of Zinc Oxide: A Combined Experimental and Theoretical Study, ChemistrySelect 2 (2017) 10038–10049.

29 A. Šarić, I. Despotović, G. Štefanić, Solvothermal synthesis of zinc oxide nanoparticles: A combined experimental and theoretical study, J. Mol. Struct. 1178 (2019) 251–260.

30 A. Šarić, I. Despotović, G. Štefanić, Alcoholic Solvent Influence on ZnO Synthesis: A Joint Experimental and Theoretical Study, J. Phys. Chem. C 123 (2019) 29394–29407.

31 J.Z. Jiang, J.S. Olsen, L. Gerward, D. Frost, D. Rubie, J. Peyronneau, Structural stability in nanocrystalline ZnO, Europhys. Lett. 50 (2000) 48–53.

32 L. Wang, H. Liu, J. Qian, Yang, Y. Zhao, Structural Stability and Compressibility Study for ZnO Nanobelts under High Pressure, J. Phys. Chem. C 116 (2012) 2074–2079.

33 Z. Dong, K.K. Zhuravlev, S.A. Morin, L. Li, S. Jin, Y. Song, Pressure-Induced Structural Transformations of ZnO Nanowires Probed by X-ray Diffraction, J. Phys. Chem. C 116 (2012) 2102–2107.

34 X. Dong, F. Liu, Y. Xie, W. Shi, X. Ye, J.Z. Jiang, Pressure induced structural transition of ZnO nanocrystals studied with molecular dynamics, Comput. Mater. Sci. 65 (2012) 450–455.

35 D. Nie, T. Xue, Y. Zhang, X. Li, Synthesis and structure analysis of aluminum doped zinc oxide powders, Sci. China Ser. B: Chem. 51 (2008) 823–828.

36 S. Cui, W. Feng, H. Hu, Z. Feng, Y. Wang, Structural and electronic properties of ZnO under high pressure, J. Alloys Compd. 476 (2009) 306–310.

37 H. Bates, W.B. White, R. Roy, New High-Pressure Polymorph of Zinc Oxide, Science 137 (1962) 993.

38 J.C. Jamieson, The phase behavior of simple compounds, Phys. Earth Planet. Inter. 3 (1970) 201–203.

39 J.M. Recio, M.A. Blanco, V. Luana, R. Pandey, L. Gerwar, J.S. Olsen, Compressibility of the high-pressure rocksalt phase of ZnO, Phys. Rev. B 58 (1998) 8949.

40 L. Gerward, J.S. Olsen, The High-Pressure Phase of Zincite, J. Synchrotron Rad. 2 (1995) 233–235.

41 H. Karzel, W. Potzel, M. Köfferlein, W. Schiessl, M. Steiner, U. Hiller, G.M. Kalvius, D.W. Mitchell, T.P. Das, P. Blaha, K. Schwarz, M.P. Pasternak, Lattice dynamics and hyperfine interactions in ZnO and ZnSe at high external pressures, Phys. Rev. B 53 (1996) 11425– 11438.

42 S. Desgreniers, High-density phases of ZnO: Structural and compressive parameters, Phys. Rev. B 58 (1998) 14102–14105.

43 H. Liu, Y. Ding, M. Somayazulu, J. Qian, J. Shu, D. Häusermann, H. Mao, 2005. Rietveld refinement study of the pressure dependence of the internal structural parameter u in the wurtzite phase of ZnO, Phys. Rev. B. 71, 212103.

44 Q. Wang, S. Li, Q. He, W. Zhu, D. He, F. Peng, L. Lei, L. Zhang, Q. Zhang, L. Tan, X. Li, X. Li, Reciprocating Compression of ZnO Probed by X-ray Diffraction: The Size Effect on Structural Properties under High Pressure, Inorg. Chem. 57 (2018) 5380–5388.

45 H.K. Mao, J. Xu, P.M. Bell, Calibration of the ruby pressure gauge to 800 kbar under quasi-hydrostatic conditions, J. Geophys. Res. 91 (1986) 4673–4676.

46 A.P. Hammersley, S.O. Svensson, M. Hanfland, A.N. Fitch, D. Häusermann, Two-dimensional detector software: From real detector to idealised image or two-theta scan, High Pres. Res. 14 (1996) 235–248.

47 H.M. Rietveld, A profile refinement method for nuclear and magnetic structures, J. Appl. Crystallogr. 2 (1969) 65–71.

48 X′Pert HighScore Plus Program, ver. 4.1; PANalytical B. V.: Almelo, Netherlands, 2014.

49 H. Toby, R. B. Von Dreele, GSAS-II: the genesis of a modern open-source all purpose crystallography software package, J. Appl. Cryst. 46 (2013) 544−549.

50 R.J. Hill, C.J. Howard, Quantitative Phase Analysis from Powder Diffraction Data using the Rietveld Method, J. Appl. Cryst. 20 (1987) 467−474.

51 R.J. Angel, High-Temperature and High-Pressure Crystal Chemistry, in R.M. Hazen, R.T. Downs (Eds.), Reviews in Mineralogy and Geochemistry, Mineralogical Society of America & Geochemical Society, 2000, pp. 35.

52 J. Gonzalez-Platas, M. Alvaro, F. Nestola, R.J. Angel, EosFit7-GUI: a new graphical user interface for equation of state calculations, analyses and teaching, J. Appl. Cryst. 49 (2016) 1377−1382.

53 U.I. Gaya, Heterogeneous Photocatalysis Using Inorganic Semiconductor Solids, Springer, Dordrecht, 2014.

54 P. Sangpour, F. Hashemi, A.Z. Moshfegh, Photoenhanced Degradation of Methylene Blue on Cosputtered M:TiO_2 (M = Au, Ag, Cu) Nanocomposite Systems: A Comparative Study, J. Phys. Chem. C 114 (2010) 13955−13961.

55 R. Hesse, T. Chasse, R. Szargan, Peak shape analysis of core level photoelectron spectra using UNIFIT for WINDOWS, Fresenius. J. Anal. Chem. 365 (1999) 48−54.

56 M.J. Frisch, G.W. Trucks, H.B. Schlegel, G.E. Scuseria, M.A. Robb, J.R. Cheeseman, G. Scalmani, V. Barone, B. Mennucci, G.A. Petersson, H. Nakatsuji, M. Caricato, X. Li, H.P. Hratchian, A.F. Izmaylov, J. Bloino, G. Zheng, J.L. Sonnenberg, M. Hada, M. Ehara, K. Toyota, R. Fukuda, J. Hasegawa, M. Ishida, T. Nakajima, Y. Honda, O. Kitao, H. Nakai, T. Vreven, J.A. Montgomery, Jr, J.E. Peralta, F. Ogliaro, M. Bearpark, J.J. Heyd, E. Brothers, K. N. Kudin, V.N. Taroverov, R. Kobayashi, J. Normand, K. Raghavachari, A.

Rendell, J.C. Burant, S.S. Iyengar, J. Tomasi, M. Cossi, N. Rega, J.M. Millam, M. Klene, J.E. Knox, J.B. Cross, V. Bakken, C. Adamo, J. Jaramillo, R. Gomperts, R.E. Stratmann, O. Yazyev, A.J. Austin, R. Cammi, C. Pomelli, J.W. Ochterski, R.L. Martin, K. Morokuma, V.G. Zakrzewski, G.A. Voth, P. Salvador, J.J. Dannenberg, S. Dapprich, A.D. Daniels, Ö. Farkas, J.B. Foresman, J.V. Ortiz, J. Cioslowski, D.J. Fox, Gaussian 09, Revision D.01, Gaussian, Inc., Wallingford CT, 2009.

57 M. Chen, T.P. Straatsma, Z. Fang, D.A. Dixon, Structural and Electronic Property Study of (ZnO)n, n ≤ 168: Transition from Zinc Oxide Molecular Clusters to Ultrasmall Nanoparticles, J. Phys. Chem. C 120 (2016) 20400−20418.

58 A.V. Marenich, C.J. Cramer, D.G. Truhlar, Universal Solvation Model Based on Solute Electron Density and on a Continuum Model of the Solvent Defined by the Bulk Dielectric Constant and Atomic Surface Tensions, J. Phys. Chem. B 113 (2009) 6378−6396.

59 Y. Zhao, N.E. Schultz, D.G. Truhlar, Design of Density Functionals by Combining the Method of Constraint Satisfaction with Parametrization for Thermochemistry, Thermochemical Kinetics, and Noncovalent Interactions, J. Chem. Theory Comput. 2 (2006) 364−382.

60 P.J. Hay, W.R. Wadt, Ab initio effective core potentials for molecular calculations. Potentials for the transition metal atoms Sc to Hg, J. Chem. Phys. 82 (1985) 270–283.

61 R.F.W. Bader, Atoms in Molecules: a Quantum Theory, Clarendon Press, Oxford, 1990.

62 T.A. Keith, AIMAll (Version 17.01.25). TK Gristmill Software, Overland Park KS, USA, 2017.

63 F. Decremps, F. Datchi, A.M. Saitta, A. Polian, S. Pascarelli, A. Di Cicco, J.P. Itié, F. Baudelet, 2003. Local structure of condensed zinc oxide, Phys. Rev. B. 68, 104101.

64 G.J. Hanna, S.T. Teklemichael, M.D. McCluskey, L. Bergman, J. Huso, 2011. Equations of state for ZnO and MgZnO by high pressure x-ray diffraction, J. Appl. Phys. 110, 073511.

65 X. Wu, Z. Wu, Lin Guo, C. Liu, J. Liu, X. Li, H. Xu, Pressure-induced phase transformation in controlled shape ZnO nanorods, Solid State Commun. 135 (2005) 780−784.

66 X. Yan, H. Dong, Y. Li, C. Lin, C. Park, D. He, W. Yang, 2016. Phase transition induced strain in ZnO under high pressure, Sci. Rep. 6, 24958.

67 S. Limpijumnong, W.R. Lambrecht, Homogeneous strain deformation path for the wurtzite to rocksalt high-pressure phase transition in GaN, Phy. Rev. Lett. 86 (2001) 91– 94.

68 K. Inoue, Ph. D. Thesis, University of Tokyo, Tokyo, 1975, 89.

69 C. Kittel, Introduction to Solid State Physics, eighth ed., John Wiley & Sons, 2004.

70 M.H. Manghnani, S- Akimoto, High-Pressure Research: Applications in Geophysics, Eds.) Academic Press, New York, 1977.

71 E. Ito, Y. Matsui, High-pressure synthesis of $ZnSiO_3$ ilmenite, Phys. Earth Planet. Inter. 9 (1974) 344–352.

72 S.H. Tolbert, A.P. Alivisatos, Size dependence of a first order solid-solid phase transition: the wurtzite to rock salt transformation in CdSe nanocrystals, Science 265 (1994) 373.

73 S.H. Tolbert, A.P. Alivisatos, The wurtzite to rock salt structural transformation in CdSe nanocrystals under high pressure, J. Chem. Phys. 102 (1995) 4642–4656.

74 S.H. Tolbert, A.B. Herhold, L.E. Brus, A.P. Alivisatos, Pressure-induced structural transformations in Si nanocrystals: surface and shape effects, Phys. Rev. Lett. 76 (1996) 4384–4387.

75 S.B. Qadri, J. Yang, B.R. Ratna, E.F. Skelton, J.Z. Hu, Pressure induced structural transitions in nanometer size particles of PbS, Appl. Phys. Lett. 69 (1996) 2205–2207.

76 J.Z. Jiang, L. Gerward, D. Frost, R. Secco, J. Peyronneau, J.S. Olsen, Grain-size effect on pressure-induced semiconductor-to-metal transition in ZnS, J. Appl. Phys. 86 (1999) 6608–6610.

77 Y.F. Chen, C.Y. Lee, M.Y. Yeng, H.T. Chiu, The effect of calcination temperature on the crystallinity of TiO_2 nanopowders, J. Cryst. Growth 247 (2003) 363–370.

78 A.P. Alivisatos, Perspectives on the Physical Chemistry of Semiconductor Nanocrystals, J. Phys. Chem. 100 (1996) 13226–13239.

79 H. Marquardt, L. Miyagi, Slab stagnation in the shallow lower mantle linked to an increase in mantle viscosity, Nat. Geosci. 8 (2015) 311–314.

80 T. Kubo, E. Ohtani, T. Kato, T. Shinmei, K. Fujino, Effects of Water on the α-β Transformation Kinetics in San Carlos Olivine, Science 281 (1998) 85–87.

81 J.L. Mosenfelder, J.A.D. Connolly, D.C. Rubie, M. Liu, Strength of (Mg,Fe)2SiO4 wadsleyite determined by relaxation of transformation stress, Phys. Earth Planet. Inter. 120 (2000) 63–78.

82 Y. Ma, Y.C. Chang, J.Z. Yin, Evaluation of lattice strain in ZnO thin films based on Williamson-Hall analysis, J. Optoelectron. Adv. M. 21 (2019) 702–709.

83 R. Ghosh, D. Basak, S. Fujihara, Effect of substrate-induced strain on the structural, electrical, and optical properties of polycrystalline thin films, J. Appl. Phys. 96 (2004) 2689 –2692.

84 K.J. Laidler, J.H. Meiser, *Physical Chemistry*, Benjamin/Cummings, 1982, p.780.

85 S. Cho, S.-H. Jung, K.-H. Lee, Morphology-controlled growth of ZnO nanostructures using microwave irradiation: From basic to complex structures, J. Phys. Chem. C 112 (2008) 12769–12776.

86 B. Ludi, M. Niederberger, Zinc oxide nanoparticles: chemical mechanisms and classical and non-classical crystallization, Dalton Trans. 35 (2013) 12554–12568.

87 M. Huang, S. Weng, B. Wang, J. Hu, X. Fu, P. Liu, Various Facet Tunable ZnO Crystals by a Scalable Solvothermal Synthesis and Their Facet-Dependent Photocatalytic Activities, J. Phys. Chem. C. 118 (2014) 25434–25440.

88 R. Saleh, N.F. Djaja, Transition-metal-doped ZnO nanoparticles: Synthesis, characterization and photocatalytic activity under UV light, Spectrochim. Acta Part A 130 (2014) 581–590.

89 C. Cheng, A. Amini, C. Zhu, Y. Xu, H. Song, N. Wang, 2014. Enhanced photocatalytic performance of TiO2-ZnO hybrid nanostructures, Sci. Rep., 4, 4181.

90 G. Kale, S. Arbuj, U. Kawade, S. Rane, J. Ambekar, B. Kale, Synthesis of porous nitrogen doped zinc oxide nanostructures using a novel paper mediated template method and their photocatalytic study for dye degradation under natural sunlight, Mater. Chem. Front. 2 (2018) 163–170.

91 W. Han, L. Ren, X. Qi, Y. Liu, X. Wei, Z. Huang, J. Zhong, Synthesis of CdS/ZnO/graphene composite with high-efficiency photoelectrochemical activities under solar radiation Appl. Surf. Sci. 299 (2014) 12–18.

92 D. Chen, K. Wang, T. Ren, H. Ding, Y. Zhu, Synthesis and characterization of the ZnO/mpg-C_3N_4 heterojunction photocatalyst with enhanced visible light photoactivity Dalton Trans. 43 (2014) 13105–13114.

93 P.S. Kumar, M. Selvakumar, P. Bhagabati, B. Bharathi, S. Karuthapandian, S. Balakumar, CdO/ZnO nanohybrids: Facile synthesis and morphologically enhanced photocatalytic performance RSC Adv. 4 (2014) 32977–32986.

94 H. T. Dao, H. Makino, Enhancement in optoelectrical properties of polycrystalline ZnO thin films by Ar plasma, Mat. Sci. Semicon. Proc. 96 (2019) 46–52.

95 L. Jing, Z. Xu, X. Sun, J. Shang, W. Cai, The Surface Properties and Photocatalytic Activities of ZnO Ultrafine Particles, Appl. Surf. Sci. 180 (2001) 308–314.

96 R. Peter, K. Salamon, A. Omerzu, J. Grenzer, I. Jelovica Badovinac, I. Šarić and M. Petravić, Role of Hydrogen-Related Defects in Photocatalytic Activity of ZnO Films Grown by Atomic Layer Deposition, J. Phys. Chem. C, 124, (2020) 8861–8868.

97 A.H. Boonstra, C.A.H.A Mutsaers, Relation between the photoadsorption of oxygen and the number of hydroxyl groups on a titanium dioxide surface, J. Phys. Chem. 79 (1975) 1694–1698.

98 Y.-H. Chin, C. Buda, M. Neurock, E. Iglesia, Reactivity of Chemisorbed Oxygen Atoms and Their Catalytic Consequences During CH_4-O_2 Catalysis on Supported Pt Clusters, J. Am. Chem. Soc. 133 (2011) 15958–15978.

99 M. Wang, F. Zhang, X. Zhu, Z. Qi, B. Hong, J. Ding, J. Bao, J. Sun, C. Gao, Drifts Evidence for Facet-Dependent Adsorption of Gaseous Toluene on TiO_2 with Relative Photocatalytic Properties, Langmuir 31 (2015) 1730–1736.

100 M.S. Bakshi, How Surfactants Control Crystal Growth of Nanomaterials, Cryst. Growth Des. 16 (2016) 1104−1133.

101 M. Irani, T. Mohammadi, S. Mohebbi, Photocatalytic Degradation of Methylene Blue with ZnO Nanoparticles; a Joint Experimental and Theoretical Study, J. Mex. Chem. Soc. 60 (2016) 218−225.

102 R. Chaudhari, D. Landge, C.J. Bhongale, A new insight into the adsorption–dissolution growth mechanism of zinc oxide hollow hexagonal nanotowers, RSC Adv. 9 (2019) 20728 −20732.

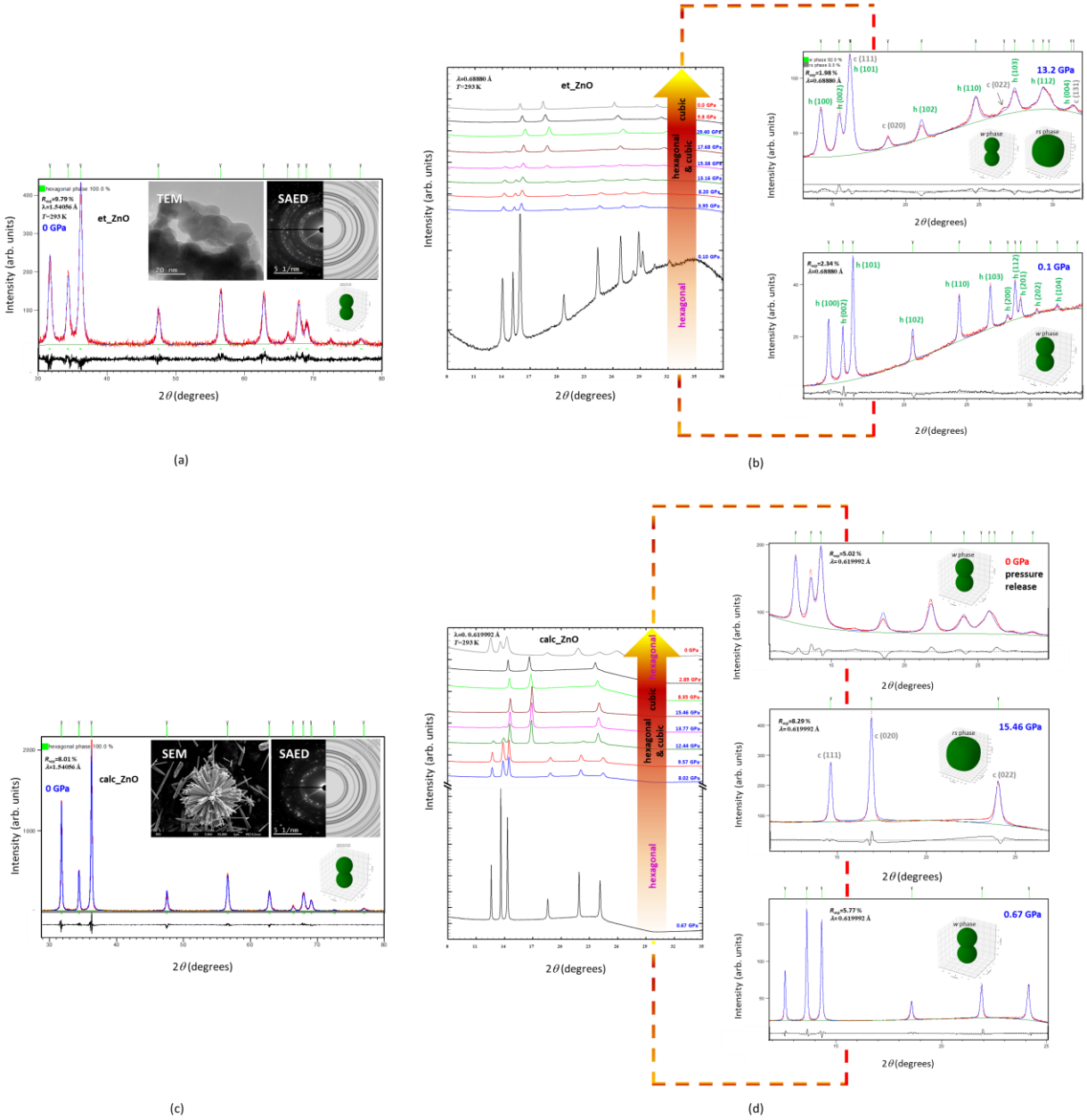
et_ZnO
0 GPa
TEM
SAED
Intensity (arb. units)
2θ(degrees)
(a)
et_ZnO
hexagonal & cubic
hexagonal
13.2 GPa
0.1 GPa
(b)
calc_ZnO
0 GPa
SEM
SAED
(c)
0 GPa
pressure release
15.46 GPa
0.67 GPa
(d)

Fig. 1.

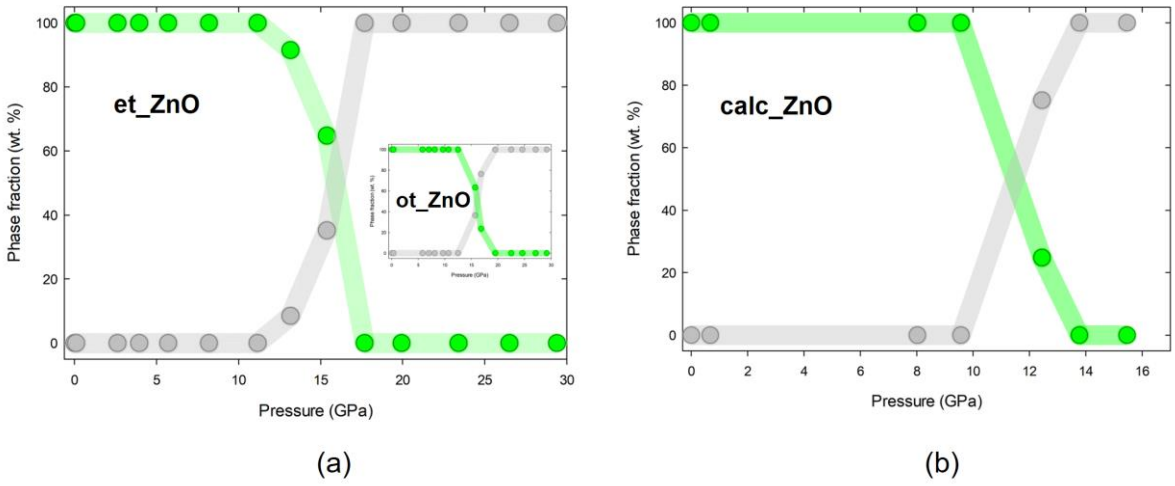
et_ZnO
ot_ZnO
calc_ZnO
Phase fraction (wt. %)
Pressure (GPa)
(a)
(b)

Fig. 2.

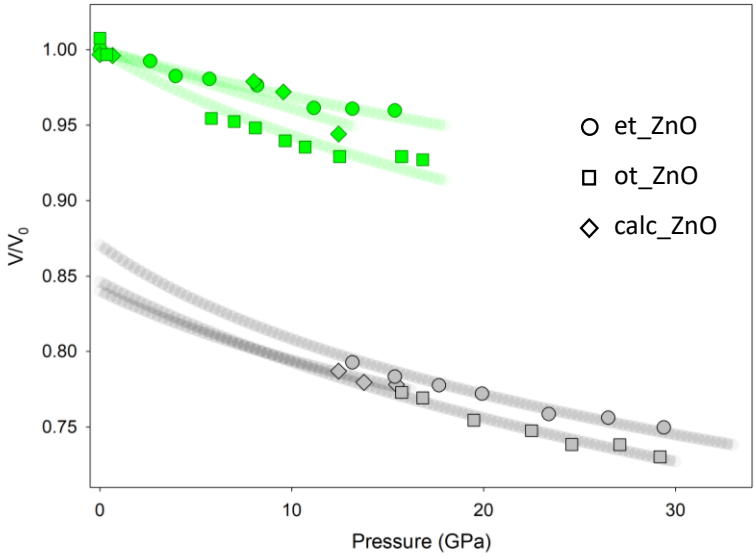
et_ZnO
ot_ZnO
calc_ZnO
V/V0
Pressure (GPa)

Fig. 3.

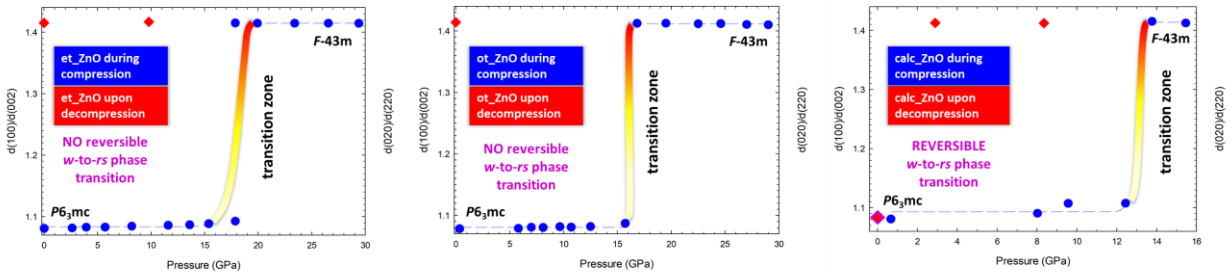
et_ZnO during compression
et_ZnO upon decompression
NO reversible w-to-rs phase transition
P6₃mc
F-43m
transition zone
d(100)/d(002)
d(020)/d(220)
Pressure (GPa)
(a)
ot_ZnO during compression
ot_ZnO upon decompression
NO reversible w-to-rs phase transition
P6₃mc
F-43m
transition zone
Pressure (GPa)
(b)
calc_ZnO during compression
calc_ZnO upon decompression
REVERSIBLE w-to-rs phase transition
P6₃mc
F-43m
transition zone
Pressure (GPa)
(c)

Fig. 4.

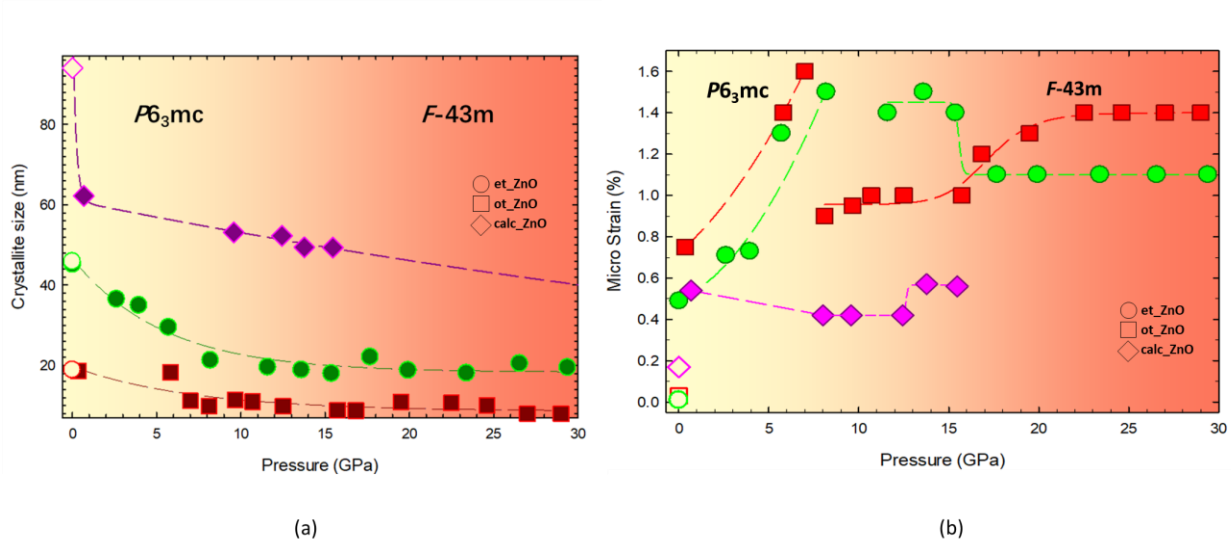
P6₃mc
F-43m
et_ZnO
ot_ZnO
calc_ZnO
Crystallite size (nm)
Pressure (GPa)
(a)
Micro Strain (%)
Pressure (GPa)
(b)

Fig. 5.

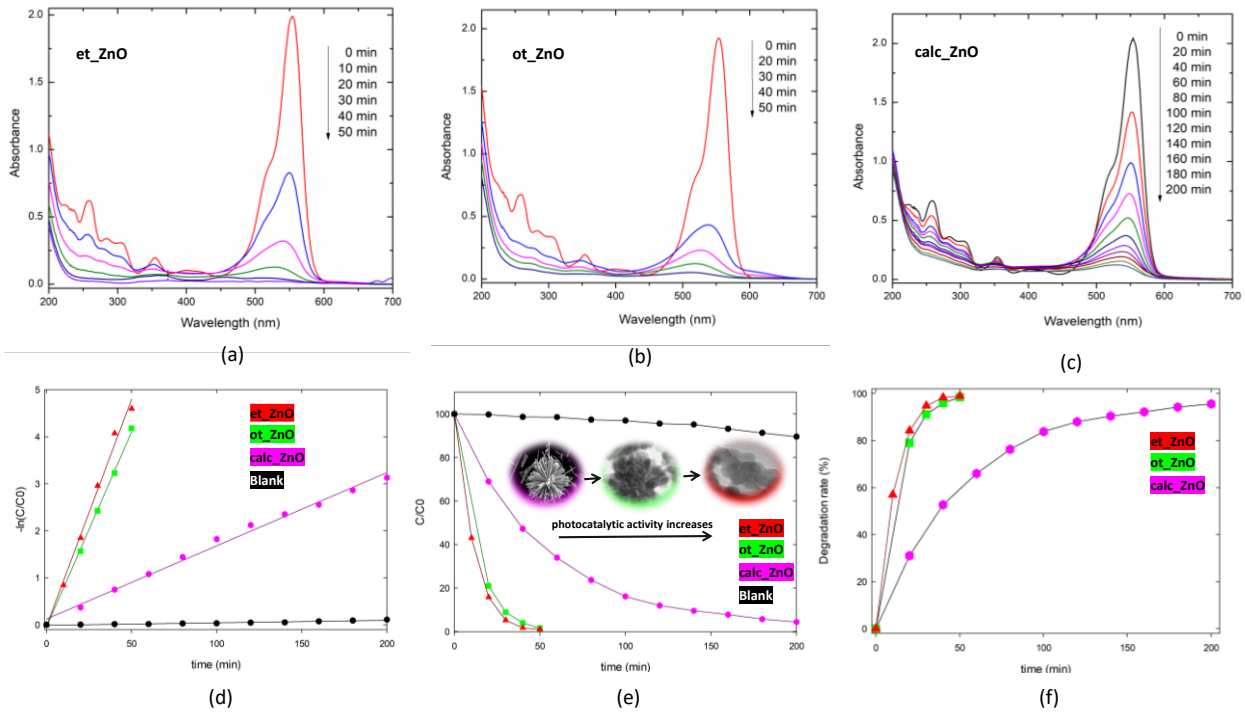
et_ZnO
0 min
10 min
20 min
30 min
40 min
50 min
Absorbance
Wavelength (nm)
(a)
ot_ZnO
0 min
20 min
30 min
40 min
50 min
Absorbance
Wavelength (nm)
(b)
calc_ZnO
0 min
20 min
40 min
60 min
80 min
100 min
120 min
140 min
160 min
180 min
200 min
Absorbance
Wavelength (nm)
(c)
et_ZnO
ot_ZnO
calc_ZnO
Blank
-ln(C/C0)
time (min)
(d)
C/C0
photocatalytic activity increases
et_ZnO
ot_ZnO
calc_ZnO
Blank
time (min)
(e)
Degradation rate (%)
et_ZnO
ot_ZnO
calc_ZnO
time (min)
(f)

Fig. 6.

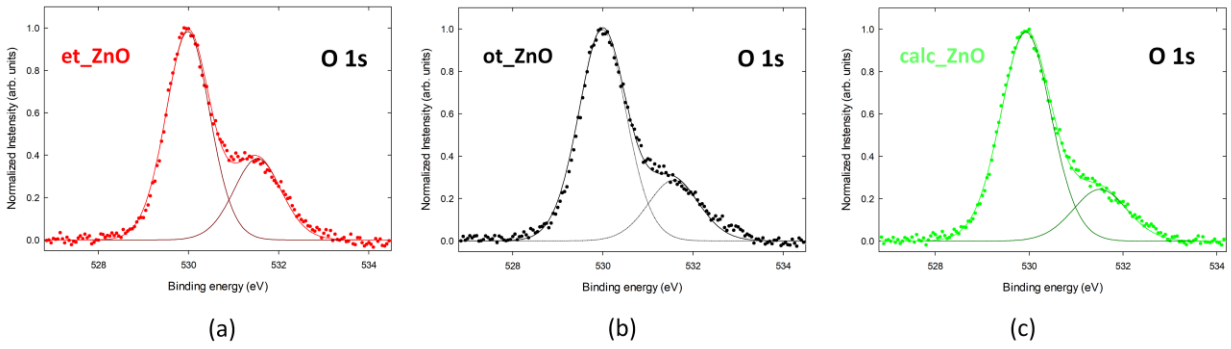
et_ZnO
O 1s
Normalized Instensity (arb. units)
Binding energy (eV)
(a)
ot_ZnO
O 1s
Normalized Instensity (arb. units)
Binding energy (eV)
(b)
calc_ZnO
O 1s
Normalized Instensity (arb. units)
Binding energy (eV)
(c)

Fig. 7.

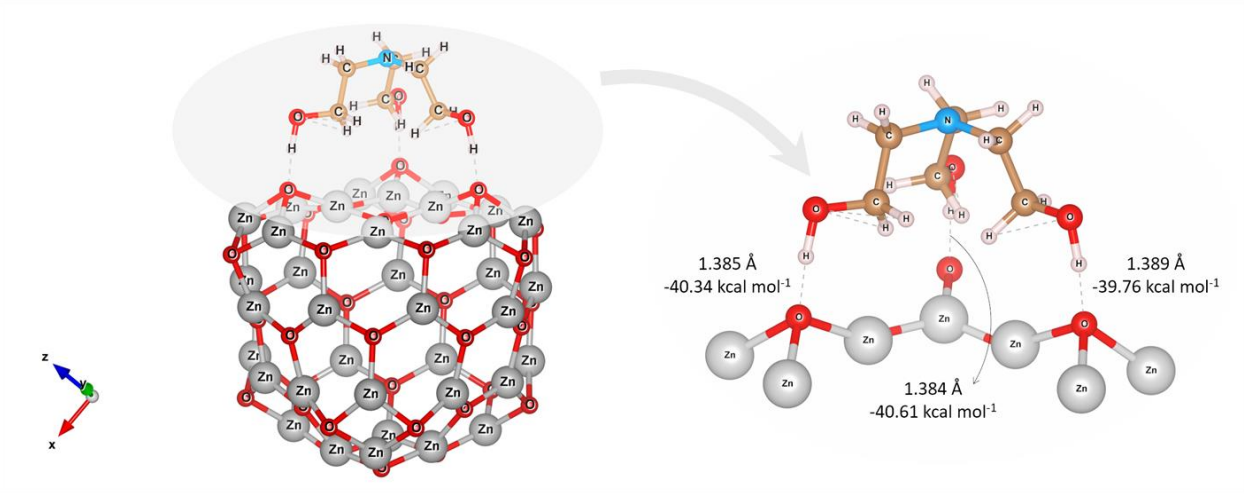

Fig. 8.

Table 1.

sample	phase	B_0 (GPa)	κ (GPa^{-1})	V_0 (Å^3)
et _ZnO	hexagonal	141(14)	0.0070	24.36(5)
	cubic	215(3)	0.0047	19.89(2)
ot_ZnO	hexagonal	130(4)	0.0077	23.74(4)
	cubic	151(2)	0.0068	19.93(3)
calc_ZnO	hexagonal	198(25)	0.0050	24.10(1)
	cubic	176(2)	0.0056	20.07(2)

Table 2.

sample	R^2	k_{app} (min^{-1})
Blank	0.94(1)	5(1)×10^{-4}
et_ZnO	0.99(6)	9.7(2)×10^{-2}
ot_ZnO	0.99(9)	8.3(4)×10^{-2}
calc_ZnO	0.99(9)	1.56(1)×10^{-2}